Control of Flow and Acoustic Fields around an Axial Fan utilizing Plasma Actuators

Hiroshi Yokoyama
Toyohashi University of Technology,
1-1, Hibarigaoka, Tempaku, Toyohashi, Aichi, 441-8580 Japan.
E-mail: h-yokoyama@me.tut.ac.jp

Nobuaki Nagao
Toyohashi University of Technology,
1-1, Hibarigaoka, Tempaku, Toyohashi, Aichi, 441-8580 Japan.
E-mail: nagao.nobuaki.ky@tut.jp

Kazuma Tokai
Toyohashi University of Technology,
1-1, Hibarigaoka, Tempaku, Toyohashi, Aichi, 441-8580 Japan.
E-mail: tokai.kazuma.dw@tut.jp

Masahito Nishikawara
Nagoya University
Furo, Chikusa, Nagoya, Aichi, 464-8603, Japan
E-mail: nishikawara@nagoya-u.jp

Abstract

Small axial fans, commonly employed for cooling electronic equipment, are frequently housed within narrow ducts, where intense tonal sound with duct resonance can occur, particularly when the blade passing frequency or its harmonic frequency aligns with the duct's resonance frequency. To mitigate resonant sound, this study proposes a flow control using dielectric barrier discharge plasma actuators, which induce a flow along the generation of plasma in air. The control effects on flow field, acoustic radiation, and aerodynamic characteristics are evaluated through direct aeroacoustic simulations and experiments conducted at different flow rates. The computational results reveal that swirling flow occurs in the inflow due to fan rotations at low flow coefficients. This swirling flow is weakened by utilizing plasma actuators, which are arranged to induce flows in the circumferentially reverse direction compared to fan rotations. This control method weakens the resonant sound at low and intermediate flow coefficients, while intensifying it at high flow coefficients, all at the same rotational speed. Moreover, the static pressure coefficient decreases and increases at low and high flow coefficients, respectively, with the latter attributed to an increase in the relative inflow angle induced by the control. Experimental findings demonstrate that the acoustic resonance was reduced by the control at both low and high flow rates, achieved by adjusting the rotational speed to maintain the same flow rate and static pressure rise as in the baseline case.

1. Introduction

Axial fans are widely used to cool electronic devices such as computers due to their ability to generate a relatively high flow rate. Both high aerodynamic performance and low noise are required for axial fans from the viewpoint of energy conservation and enhancing human working conditions.

The aerodynamic sound produced by the flow around axial fans comprises tonal and broadband sounds. Tonal sound arises at the blade passing frequency (BPF) and its harmonic frequencies due to the periodic interference between the wakes of the rotor blades and stators (struts) [1]. Additionally, the interactions of non-uniform or turbulent inflow with rotor blades also cause tonal and broadband sounds [2]. Inflow turbulence is related to reverse flows around the tip regions of a fan, where a swirling flow can be produced upstream of the fan [3].

The effects of fan installation conditions on aerodynamic performance and acoustic radiation have been extensively studied [4–6]. Longhouse [4] demonstrated that fan peak efficiency decreased with increasing clearance, with tip clearance noise contributing up to 15 dB to the overall noise. Lin et al. [5] observed that installing a blockage plate upstream of a fan resulted in static pressure loss and an increase in broadband noise. Moreover, the tonal sound at the BPF was amplified by acoustic resonance, especially when an axial fan was installed in confined spaces or narrow ducts [6].

Accordingly, several passive methodologies [7–10] have been explored to mitigate aerodynamic noise radiated from an axial fan. Naitong et al. [7] reported that acoustic radiation could be reduced by up to 10 dB(A) by installing a fan in a porous casing. Tingsheng et al. [8] demonstrated that tonal sound could be suppressed by incorporating a resonator-type silencer on the inner surface of a fan casing. Additionally, the introduction of slits in a fan casing was investigated to control tip leakage flow [9, 10]. The inflow through the slits was identified to influence the swirling flow around the fan, thereby weakening the acoustic radiation associated with the interactions between circumferentially-convected tip vortices and blades. This indicates that controlling the circumferential flow around the fan can be effective in controlling the acoustic radiation from an axial fan. However, the effectiveness of slit arrangement in a casing is compromised when a fan is installed in a narrow duct, as the inflow through the slits is impeded under such conditions [10].

Active flow control has emerged as a promising approach for reducing fan noise under various fan installation conditions. Neuhaus et al. [11] demonstrated that streamwise air injection near the blade tip decreased the tonal noise levels at the BPF. However, the control effects of circumferential jet on flow and acoustic radiation remain unexplored. In recent years, numerous studies have been conducted on plasma actuators as flow-control devices, as they can induce flow along the generation of plasma in air [12–15]. A dielectric barrier discharge plasma actuator comprises top and bottom electrodes, with a dielectric layer between the electrodes. A plasma sheet appears on the dielectric layer upon application of a high AC voltage to the electrodes, resulting in flow generation. Plasma actuators have found applications for various objectives, such as suppressing flow separation [12, 13] and delaying compressor stall [14]. Furthermore, a plasma actuator has been demonstrated to effectively reduce acoustic radiation from cavity flows in a previous study [15], wherein direct aeroacoustic simulations conducted alongside wind tunnel experiments. A plasma actuator offers several advantages: no moving parts, easy attachment to objects, fast response time, and low mass. Therefore, it holds significant potential as an effective method for controlling both flow and sound around axial fans installed in narrow spaces.

The objective of this study is to elucidate the efficacy of plasma actuators in controlling the acoustic radiation of resonant sound emitted by an axial fan installed in a narrow duct. For the first time, direct aeroacoustic simulations and experiments were performed for evaluating the effectiveness of plasma actuators designed to circumferentially induce jets upstream of the fan. Additionally, this study discusses the influence of plasma actuators on flow fields and aerodynamic characteristics .

Section 2 outlines the computational and experimental methodologies, along with the control methods employed in the study. In Section 3, the predicted flow induced by the plasma actuators and their impact on aerodynamic characteristics and acoustic radiation are compared with those measured for computational validation. In Section 4, computational and experimental results are presented and discussed. The baseline acoustic radiation with acoustic resonance is presented in Subsection 4.1. The control effects on the resonant sound and aerodynamic characteristics are discussed in Subsections 4.2 and 4.3, respectively. The mechanism of these control effects is discussed based on the flow field in Subsection 4.4.

2. Methodologies

2.1 Fan and Working Conditions

For the fan housed in the casing, as depicted in Fig. 1, plasma actuators were utilized for flow control. The number of rotor blades with a chord length of $C = 22.3$ mm was $Z_b = 5$, with four struts placed downstream of the rotor. The radii of the rotor and hub were $r_f = 18.5$ mm and $r_h = 9$ mm, respectively. The details of the fan have been described in a previous study [10]. The fan was arranged in a casing with an outer side of $D = 40$ mm and an inner radius of $r_c = 19.5$ mm. The tip clearance was $\sigma = r_c - r_f = 0.04C$, and the flow passage area of the fan was $A = 9.4\times10^{-4}$ m^2.

A fan enclosed in a casing was positioned in a duct featuring a square flow passage on side D (upstream duct), as shown in Fig. 2, assuming the fan’s installation in a narrow space. The outflow from the fan was directed into the downstream duct via a square flow passage with a side of $4D$, facilitated by a baffle plate with a thickness of 10 mm. The origin of the coordinates was set at the center of the front surface of the hub. As illustrated in Fig. 2, the x and y axes corresponded to the axial and vertical directions, respectively, while the z axis was normal to the x and y axes.

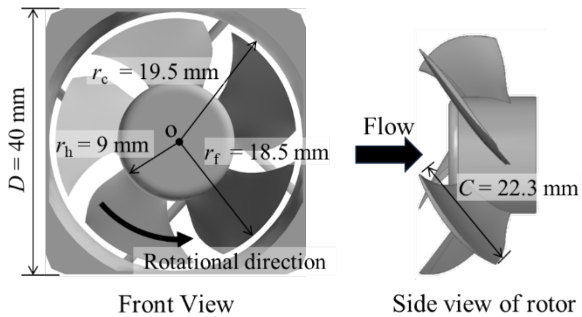

Fig. 1. Axial fan with five rotor blades housed in casing with four struts.

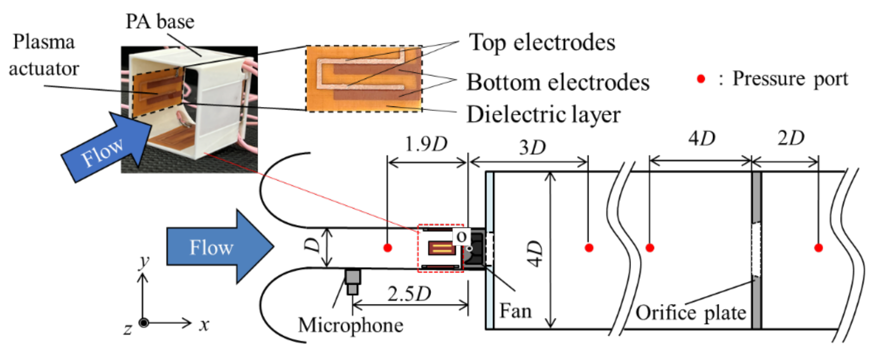

Fig. 2. Experimental setup for control of flow around a fan with plasma actuators, wherein an axial fan is installed in a duct (with a square flow passage having side of D = 40 mm).

The rotational speed was set to n = 50.4, 60.0, and 70.0 s^{-1} during the experiments to clarify the impact of rotational speed on the baseline acoustic radiation without control. The control effects of the plasma actuators were evaluated at n = 60.0 s^{-1}, where the duct resonance intensely occurred [6]. At n = 60.0 s^{-1}, the tip velocity was V_{tip} = 6.97 m/s, resulting in a Reynolds number of $\mathrm{Re} \equiv V_{tip}C/\nu = 1.04\times10^4$, where ν denotes the kinematic viscosity of air, and the Mach number was 0.02. The flow coefficient defined by $\phi \equiv Q/AV_{tip}$, where Q represents the flow rate, was varied from $\phi = 0.00$ (maximum static pressure) to $\phi \approx 0.36$ (maximum flow rate) at each rotational speed in the experiment. The computations were performed for $\phi = 0.05$, 0.17, and 0.23, corresponding to low, intermediate, and high flow rates, respectively.

2.2 Control by Plasma Actuator

Schematics of the control configurations for the flow around the fan are shown in Fig. 3. The plasma actuator, comprised of top and bottom electrodes, featured electrodes with 18-μm thickness arranged on a dielectric layer having 200-μm thickness. The widths of the top and bottom electrodes were 1 and 3 mm, respectively, based on a previous study [15]. As depicted in Fig. 3, two plasma actuators were installed in $x/D = -0.9$ to -0.35, with an 8-mm interval on four inner duct surfaces upstream of the fan. The electrodes of the plasma actuators were arranged for the induced flows to be directed in the reverse direction compared to the fan rotations, aimed at suppressing the swirling flow induced by fan rotations in the upstream region, as discussed in Subsection 4.4. The interval between actuators was determined to induce effective flows based on preliminary experiments, and a comparison of induced flows by one actuator versus two actuators is presented in Section 3. To prevent the generation of flow disturbances by the installation of plasma actuators, the plasma actuators were flush-mounted [15, 16] via a plasma-actuator (PA) base. The inner shape of the flow passage of the PA base transitioned smoothly from the square shape of the upstream duct to the circular shape of the fan casing. The plasma actuator was continuously driven with an alternating voltage of $V_{pp} = 9.4$ kV and a frequency of 4.2 kHz, following previous research protocols [17]. The temperature in the exhausted flow of the fan was confirmed to be unchanged (within 0.1 K) by the driving of the plasma actuator.

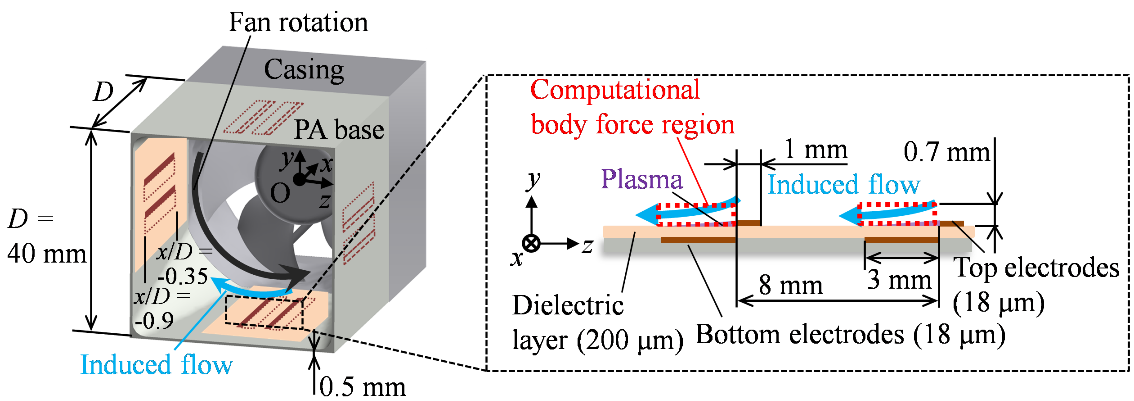

Fig. 3. Schematics of control by plasma actuators upstream of the fan.

2.3 Experimental Methodologies

2.3.1 Measurement Methods

The experimental setup and measurement methods for evaluating the aerodynamic characteristics and acoustic radiation were consistent with those employed in a prior investigation [10]. The flow rate Q was determined by measuring the pressure difference between the orifice plates installed downstream of the fan using a differential manometer (DPC-500N12, OKANO WORKS, LTD) according to ISO 5167-1. As shown in Fig. 2, the static pressure rise ΔP induced by the fan was evaluated by computing the mean pressure difference between $x/D = -1.9$ and 3.0 on the duct wall. The sampling frequency and duration were 2000 Hz and 60 s, respectively. The static pressure coefficient, defined by $\psi = 2\Delta P/\rho V_{tip}^2$, where ρ represents the density of air, was calculated based on the measured pressure rise for evaluating the aerodynamic characteristics.

The sound pressure level was measured using a microphone (NL-31, RION) positioned at $x/D = -2.5$ on the upstream duct wall, as illustrated in Fig. 2. The sampling frequency was set to $256nZ_b$ at all rotational speeds for precisely evaluating the tonal sounds at the BPF (nZ_b) and its harmonic frequencies, where the sampling time was 15 s.

The velocity fields of the flows induced by one and two plasma actuators set on a wide flat wall were measured using particle image velocimetry (PIV) as explained in Appendix B. The PIV images were captured with a shutter speed of 1 ms using a high-speed camera (FASTCAM Mini AX100, Photoron) with YAG laser (CW532-5WMUT, 5 W, Kanomax).

2.3.2 Measurement uncertainties

The primary sources of the uncertainties in the flow and pressure coefficients were the variations in measuring the pressure difference across the baffle or orifice plate, rotational speed, and fluid density. Detailed descriptions of these uncertainties are provided in Appendix A. According to literature [18], the uncertainty of the flow coefficient was estimated to be ±0.003 at $n = 60.0$ s^{-1} and $\phi = 0.17$ without control, corresponding to ±1.8% of the measured coefficient. Similarly, the uncertainty in the pressure coefficient was ±0.0007, representing ±0.3% of the measured pressure coefficient. To estimate the uncertainty in measuring the sound pressure level, the variation in the repeatability of the measured sound pressure level was examined using four tests for each condition. The variation in the sound pressure level at the BPF of nZ_b was ±0.8 dB at $n = 60.0$ s^{-1} and $\phi = 0.17$ without control.

2.4 Computational Methods

2.4.1 Governing Equations and Finite Difference Scheme

The computational schemes employed herein were identical to those utilized in previous studies [6, 10]. To directly simulate the flow and aerodynamic sound around the fans, three-dimensional compressible Navier-Stokes equations along with continuity and energy equations were solved. Spatial derivatives were evaluated using the sixth-order accurate compact finite difference scheme (the fourth-order accurate scheme at the boundary) [19]. Time integration was performed utilizing the third-order accurate Runge-Kutta method.

A volume penalization method [20, 21] was employed to reproduce rotating or complex-shaped objects, such as fans, casings, and bell-mouthed ducts, using a rectangular grid. The external force, termed the penalization term $\boldsymbol{V}$, and the body force of the plasma actuators $\boldsymbol{D}_{\mathrm{PA}}$, were incorporated to the right-hand side of the governing equations:

$$(\boldsymbol{Q}_{\mathrm{c}})_t + (\boldsymbol{E} - \boldsymbol{E}_{\mathrm{v}})_x + (\boldsymbol{F} - \boldsymbol{F}_{\mathrm{v}})_y + (\boldsymbol{G} - \boldsymbol{G}_{\mathrm{v}})_z = \boldsymbol{V} + \boldsymbol{D}_{\mathrm{PA}}, \tag{1}$$

$$\boldsymbol{V} = -\left(1/\varUpsilon - 1\right)\chi\left(\nabla \cdot \rho\boldsymbol{u} \quad 0 \quad 0 \quad 0 \quad 0\right)^{\mathrm{T}}, \tag{2}$$

$$\varUpsilon = 0.25, \tag{3}$$

$$\chi = \begin{cases} \min\left(1, \left|\theta - \theta_{\mathrm{b}}\right| / \varDelta\theta\right) & \text{(solid)} \\ 0 & \text{(fluid)} \end{cases}, \tag{4}$$

where $\boldsymbol{Q}_{\mathrm{c}}$ represents the vector of the conserved variables; $\boldsymbol{E}$, $\boldsymbol{F}$, and $\boldsymbol{G}$ denote the inviscid flux vectors; and $\boldsymbol{E}_{\mathrm{v}}$, $\boldsymbol{F}_{\mathrm{v}}$, and $\boldsymbol{G}_{\mathrm{v}}$ signify the viscous flux vectors. In the present simulation, the coefficient $\varUpsilon$ was determined to be 0.25, such that sound waves were almost completely reflected (reflectivity: 99%) on the objects without computational unsteadiness [22]. The variable χ is the mask function. It was set as zero outside the solid and one inside the solid, except for the region near the surface of the blade. The mask function was determined based on the circumferential angle from the surface, $\theta - \theta_b$, as shown in Eq. (4), where θ_b represents the angle of the nearest blade surface and $\Delta\theta$ denotes the angle between neighboring grid points.

Large-eddy simulations were performed to clarify the unsteady flow and acoustic fields without excessive computational costs, and no explicit subgrid-scale (SGS) model was used. A tenth-order spatial filter [23] dissipated the turbulence energy at the grid scale, which was then transferred to the SGS eddies [10, 24, 25]. The filter also suppressed the numerical instabilities associated with central differencing in the compact scheme.

The body force of the plasma actuators was applied in the computational region near the plasma actuator, as shown in Fig. 3, and is expressed as:

$$\boldsymbol{D}_{\mathrm{PA}} = -F_{\mathrm{PA}} \boldsymbol{p}_{\theta}, \tag{5}$$

where $\boldsymbol{p}_\theta$ denotes the circumferential unit vector in the fan rotational direction perpendicular to the normal vector of each duct wall. The magnitude of the body force $F_{\mathrm{PA}}/(\rho V_{\mathrm{tip}}^2/2C)$ was set to 0.011, which was determined based on the measured velocity profile around the plasma actuator in the preliminary computations. A comparison of the predicted and measured profiles of the flow induced by the plasma actuators is presented in Subsection 3.1.

2.4.2 Computational Domain

Figure 4 illustrates the computational domain, encompassing the region in and around the bell-mouthed upstream duct with a fan and a downstream duct. The computational region was divided into flow, sound, and buffer regions. The grid spacing smoothly changed between regions. In the flow region, flow structures, such as the boundary layer, wake, and vortices around the rotating blades and struts, were captured by the minimum grid spacing of Δ_{min}/D = 1/400 (Δ_{min}/C = 1/220). This grid resolution was identical to that employed in previous studies [6, 10], where the flow and acoustic fields from the present axial fan were correctly captured. In a previous study [10], the numerical uncertainty in the static pressure coefficient of the fan with the present grid was estimated to be 5% based on the grid convergence index (GCI) method [26].

Acoustic propagation was accounted for in the sound region, extending to 34D, corresponding to one acoustic wavelength of the BPF at n = 60.0 s^{-1} (300 Hz). The maximum grid width in the sound region was Δ/D = 0.4, ensuring at least eight grid points per one acoustic wavelength for the frequency range of $f \leq 6nZ_b$ (1800 Hz for n = 60.0 s^{-1}), thereby facilitating accurate prediction of acoustic propagation [10, 15, 19]. In the buffer region, grid width was stretched to Δ/D = 25 to weaken acoustic waves near artificial inflow and outflow boundaries. The total number of grid points in the computational domain was 300 million.

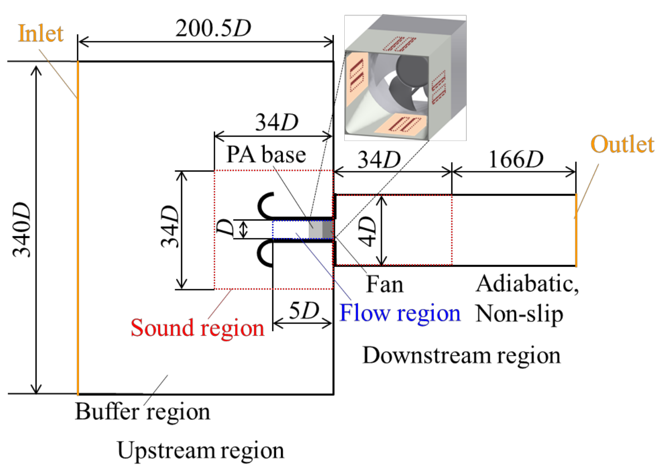

Fig. 4. Computational domain with boundary conditions.

2.4.3 Boundary Conditions and Initial Flow Field

Non-slip and adiabatic conditions were set for the duct and baffle plate walls. Non-reflecting boundary conditions were imposed on the far artificial inlet and outlet boundaries for the smooth passage of acoustic disturbances [27].

For the baseline case without control, the computational results were analyzed using the data after flow development during 20 blade-passing periods from the initial stationary flow field. Computations controlled by the plasma actuator were performed by setting the developed baseline flow field as the initial flow field. A spectral analysis was performed using the computational results during 20 blade-passing periods from the developed flow field, where the average number of spectra was approximately 10 under all conditions.

3. Comparison of Computational and Experimental Results

3.1 Induced Flow by Plasma Actuator(s)

The predicted velocity fields of the induced flows by one and two plasma actuators on a wide flat plate of $2.5D\times2.5D$ (100×100 mm^2), as shown in Fig. 5(a), were compared with those measured by the particle image velocimetry (PIV) explained in Appendix B. Figure 5(b) depicts the measured and predicted velocity profiles 5 mm downstream of the plasma actuators. The data uncertainties due to the spatial resolution concerning the interrogation area in the PIV (0.46 mm), alongside the frame interval for the calculation of cross-correlation (1 ms), are shown as error bars in the experimental data. The predicted profiles with one and two plasma actuator(s) approximately agreed with the measured values.

As illustrated in Fig. 5(b), the velocity profile predicted with the above-mentioned present grid resolution (Δ_{min}/D = 1/400) for one plasma actuator was also compared with the finer grid resolution (Δ_{min}/D = 1/800). The approximate agreement between these two profiles indicates that the present grid resolution was sufficiently fine to adequately capture the induced flow with the plasma actuator. The predicted maximum velocities around a distance of 0.7 mm from the wall were 0.74 and 0.94 m/s for one and two plasma actuators, respectively. This confirms that the induced flow with two plasma actuators with the present interval of 8 mm was intensified compared to that with one actuator.

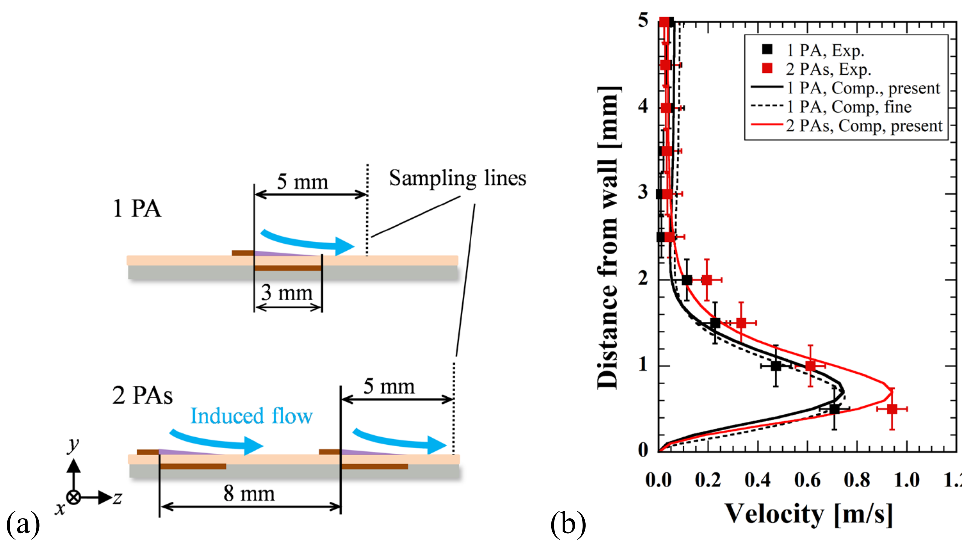

Fig. 5. Comparison of measured and predicted velocity fields of induced flow by one and two plasma actuators on a wide flat plate. (a) Setup of plasma actuators. (b) Measured and predicted velocity profiles 5 mm downstream of the plasma actuators.

3.2 Aerodynamic characteristics

Figure 6 presents the baseline and controlled variations of the static pressure coefficient with flow coefficient at n = 60.0 s^{-1}, where the measurement uncertainties of the flow coefficients discussed in Subsection 2.3.2 are indicated. As shown in Fig. 6, the static pressure coefficient generally increased as the flow coefficient decreased from the maximum flow rate of ϕ = 0.36. The gradient of the increase became relatively small around ϕ = 0.20 compared with other flow coefficients, which occur owing to the interactions of tip vortices with the pressure surfaces of a neighboring blade as reported in a previous study [10]. Both the baseline and controlled pressure coefficients predicted by the present simulations agree approximately with the measured values. Specifically, the measured static pressure coefficient increased under control at relatively high flow coefficients of $\phi \geq 0.18$, while it decreased under control at lower flow coefficients. These control effects were accurately predicted in the present simulations, where the static pressure coefficient was decreased at ϕ = 0.05 and 0.17 and increased at ϕ = 0.23.

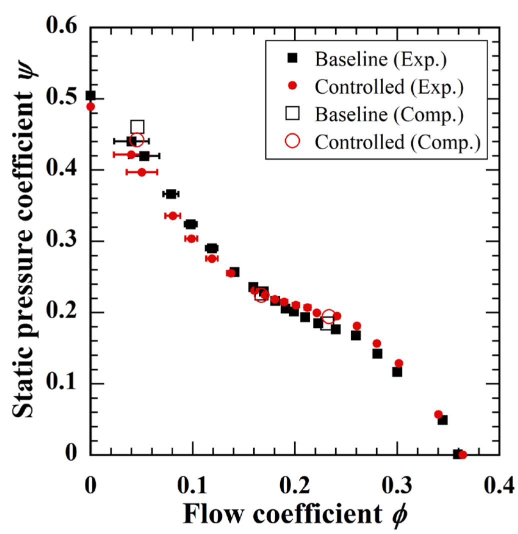

Fig. 6. Measured and predicted variations of static pressure coefficient with flow coefficient for baseline and controlled flows at n = 60.0 s^{-1}.

3.3 Acoustic Radiation

Figure 7 shows the measured and predicted sound pressure spectra (x/D = −2.5) with and without control at n = 60.0 s^{-1} and ϕ = 0.05, where the frequency resolution was $\Delta f/nZ_b$ = 1/4 and the data were averaged 10 and 2250 times in time for the computation and experiment, respectively. The variances in the measured levels with the same average number as that of the computation are represented by bars. The predicted levels were within the measured variances in both cases, with and without the control. In the baseline case, an intense tonal sound occurred at the first harmonic frequency of the BPF ($2nZ_b$, 600 Hz), which corresponded to the duct resonance frequency of the upstream duct [6]. Both the predicted and measured spectra indicate that the resonant tonal sound was weakened by the control.

Considering the measured and predicted flow fields, aerodynamic characteristics, and acoustic radiation, it can be concluded that the present computations can capture the flow field, acoustic radiation with duct resonance, and aerodynamic characteristics of the axial fan with the control of plasma actuators.

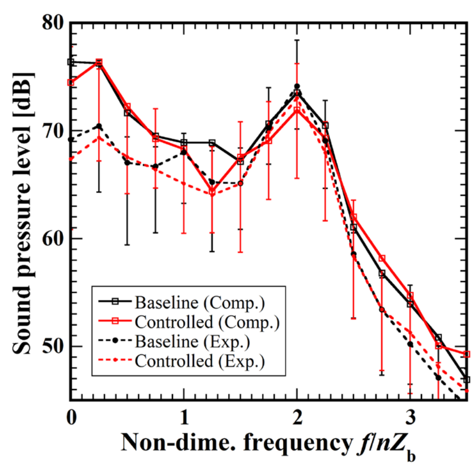

Fig. 7. Measured and predicted sound pressure spectra with and without control at n = 60.0 s^{-1} and $\phi = 0.05$, where variances of measured level with the same averaging number as that of the computation are represented with bars.

4. Results and Discussions

4.1 Baseline Radiation with Acoustic Resonance

Figure 8 shows the measured sound pressure spectra at different rotational speeds at the flow coefficient of $\phi = 0.17$, in which the frequency resolution is $\Delta f/nZ_b = 1/256$, corresponding to $\Delta f = 0.98$, 1.17, and 1.37 Hz for $n = 50.4$, 60.0, and 70.0 s^{-1}, respectively.

It was shown that an intense sound occurred at 600 Hz, independent of the rotational speed. This frequency agreed with that of the acoustic resonance with a one-quarter wavelength mode in the axial direction of the upstream duct [6]. This resonant sound became most intense at $n = 60.0\ \mathrm{s}^{-1}$, owing to the agreement of the resonance frequency with the first harmonic frequency of the BPF ($2nZ_b$).

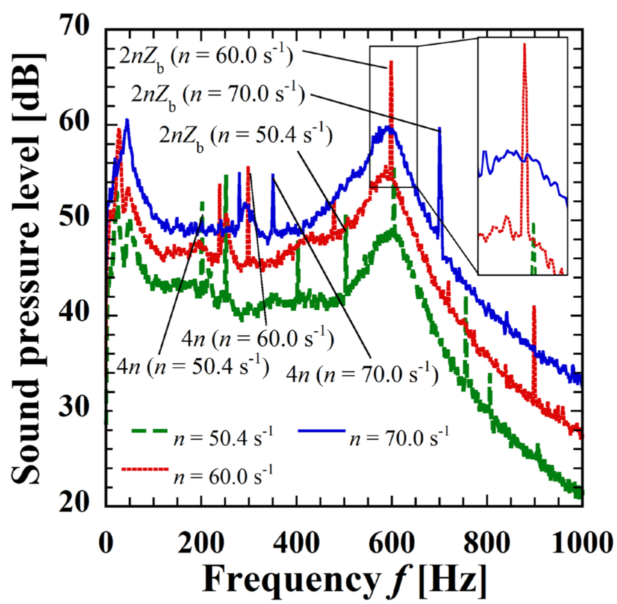

Fig. 8. Measured baseline sound pressure spectra at $x/D = -2.5$ for $\phi = 0.17$, wherein the frequency resolution is $\Delta f/nZ_b = 1/256$ corresponding to $\Delta f = 0.98$, 1.17, and 1.37 Hz for $n = 50.4$, 60.0, and $70.0\ \mathrm{s}^{-1}$, respectively.

The predicted contours of the fluctuation pressure, which is the instantaneous pressure with mean pressure subtracted, $p' = p - P$, in and around the upstream duct for the baseline flow at $n = 60.0\ \mathrm{s}^{-1}$, are shown in Fig. 9. Time $t = 0$ is for the highest pressure, and T is the time period of the above-mentioned resonance frequency. It is shown that the compression and expansion waves are periodically generated at the resonance frequency in the upstream duct, causing the formation of standing waves.

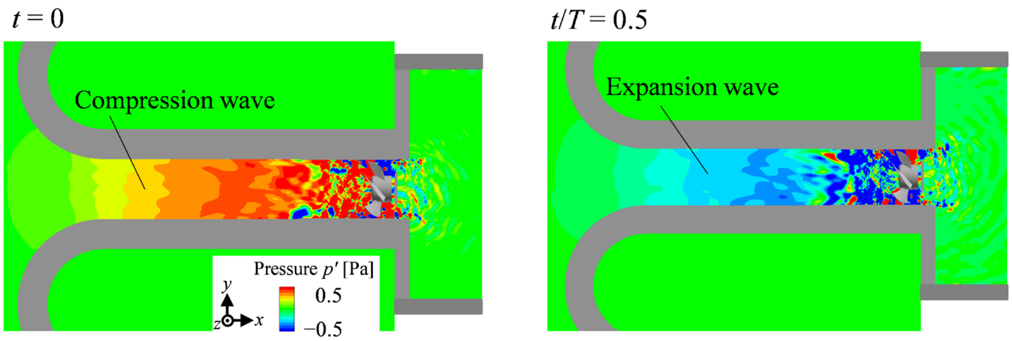

Fig. 9. Predicted contours of fluctuations pressure without control at n = 60.0 s^{-1} and ϕ = 0.05, where t = 0 is time for the highest fluctuation pressure in the upstream duct and T is time period of resonance frequency.

4.2 Control Effects on Acoustic Radiation

Figure 10 depicts the difference between the sound pressure level of the resonant sound at $2nZ_b$ with control and that without control at n = 60.0 s^{-1}, where the measured and predicted results are shown. The level of the resonant sound was estimated by integrating the acoustic power in the frequency range in which the difference in the level from the peak level at $2nZ_b$ was within 5 dB. The variances in the levels of the four tests are shown as bars for the measured data. As shown in Fig. 10, the measured resonant sound was weakened at relatively low flow coefficients of $\phi \leq 0.17$, while that was intensified at higher flow coefficients of $\phi \geq 0.23$. The predicted difference is also shown to be along the measured difference.

Figure 11 shows the predicted contours of the fluctuation pressure in and around the upstream duct for the controlled flow with n = 60.0 s^{-1} and ϕ = 0.05. Compared with the baseline contours shown in Fig. 9, the compression and expansion waves generated in the upstream duct weakened. This confirms the weakening of the acoustic resonance in the upstream duct by control using plasma actuators.

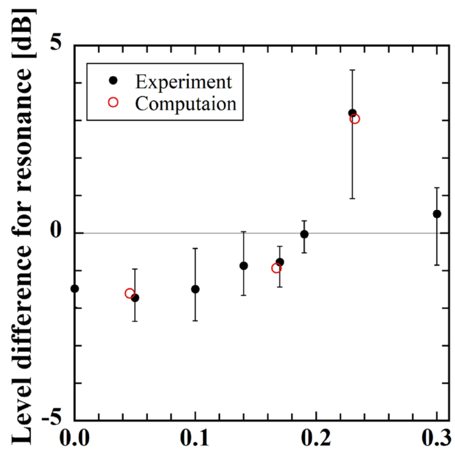

Fig. 10. Measured and predicted variations of the level difference of baseline and controlled resonant sounds at $2nZ_b$ with flow coefficient (n = 60.0 s^{-1}, x/D = −2.5), where variances of level in four tests are indicated with bars for measured data.

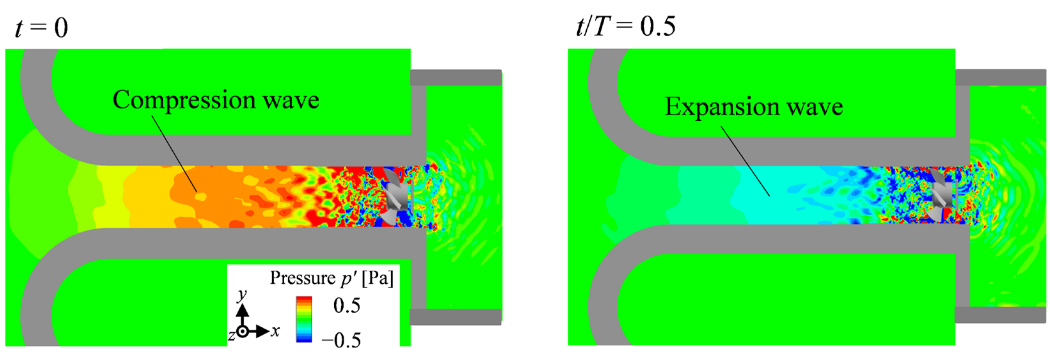

Fig. 11. Predicted contours of fluctuating pressure in and around the upstream duct for controlled flow at ϕ = 0.05 and n = 60.0 s^{-1}.

4.3 Discussions of Control Effects on Aerodynamic Characteristics

Figure 12 shows the mean pressure difference between pressure and suction surfaces, $P_p - P_s$, along the 80% span of the rotor blades. The horizontal axis represents the non-dimensional chordwise position x_c, where x_c = 0.0 and 1.0 correspond to the leading and trailing edges, respectively. As shown in Fig. 12, the high blade loading occurs around $x_c \approx 0.1$, which is decreased and increased by the control at ϕ = 0.05 and 0.23, respectively. This is consistent with the control effects on the aerodynamic characteristics shown in Fig. 6, where the static pressure coefficient was decreased and increased for $\phi \geq 0.18$ and $\phi \leq$

0.17, respectively. The mechanism for the control effects on the aerodynamic characteristics is discussed based on the change in the flow fields upstream of the fan with the control in Subsection 4.4.

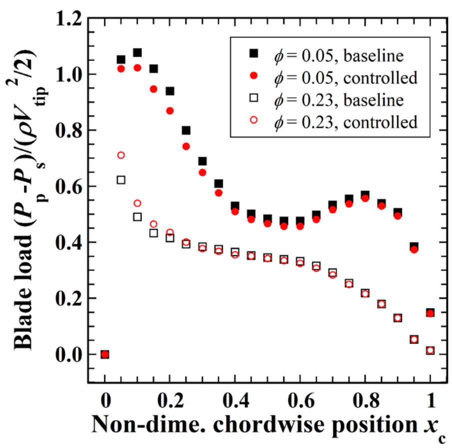

Fig. 12. Predicted blade loading along 80% span for baseline and controlled flows with ϕ = 0.05 and 0.23, where x_c = 0.0 and 1.0 correspond to leading and trailing edges, respectively.

Considering the actual application of the axial fan for necessary flow generation in industrial parts, the sound pressure level was measured in the controlled flow with adjusted rotational speeds for the same flow rate and static pressure conditions as those of the baseline flow at $n = 60.0$ s^{-1}. Figure 13 shows the measured levels of the resonant sound at $2nZ_b$ in the spectra with $\Delta f/nZ_b = 1/256$ at $n = 63.0$ s^{-1} and 57.0 s^{-1} for the aerodynamic conditions of $\phi = 0.05$ and 0.23 at $n = 60.0$ s^{-1}, respectively, along the baseline levels (n = 60.0 s^{-1}). This figure shows that the sound pressure level was reduced by 4.7 dB and 0.5 dB at the low and high flow rate conditions, corresponding to $\phi = 0.05$ and 0.23 at $n = 60.0$ s^{-1}, respectively. This reduction occurred because the rotational condition was separated from the resonance condition, in which the harmonic frequency of the BPF became different from the resonance frequency of the upstream duct [6]. Moreover, the weakening of velocity fluctuations at the BPF in the rotor wake contributed to the sound reduction at the harmonic frequency for ϕ = 0.05 as discussed in Subsection 4.4.3. The overall sound pressure level in the frequency range of 0.3–4.0nZ_b was 75 dB and 78 dB at ϕ = 0.05 and 0.23, respectively, which was found to be unchanged between the baseline and controlled cases. These results indicate that the proposed control using plasma actuators successfully reduces the intense resonant noise at the harmonic frequency of the BPF under the equivalent pneumatic power generated by the fan.

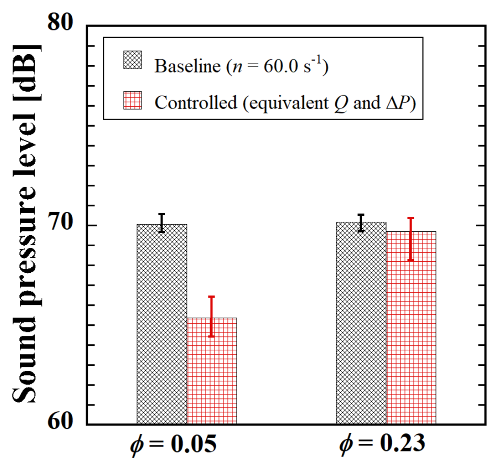

Fig. 13. Levels of resonant sound at 2nZ_b in controlled flows with adjusted rotational speeds of n = 63.0 s^{-1} and 57.0 s^{-1} for the same flow rate and static pressure as those in baseline case at ϕ = 0.05 and 0.23 at n = 60.0 s^{-1}, respectively, along baseline levels.

4.4 Flow Fields around Axial Fan

4.4.1 Swirling Flow in Inflow to Fan

The predicted contours of mean circumferential velocity, V_θ, upstream of the fan (x/D = −0.35) with and without control are shown in Fig. 14(a). Swirling flow in the rotational direction of the fan was shown to occur, particularly near the duct walls, and was weakened by the control. Figure 14(b) shows the baseline and controlled profiles of the mean circumferential velocity with distance from the wall h in the normal directions of the duct walls, where the values were averaged in four lines, as shown by broken lines in Fig.

14(a). The circumferential velocity decreased at ϕ = 0.05 by the control, which indicates the weakening of the swirling upstream of the fan. Meanwhile, the intense circumferential velocity did not occur in the baseline flow at the high flow coefficient of ϕ = 0.23. The control induced a reverse swirling flow upstream of the fan, which resulted in a rise in the relative inflow angle, leading to increase in static pressure coefficient and blade loading as shown in Figs. 6 and 12.

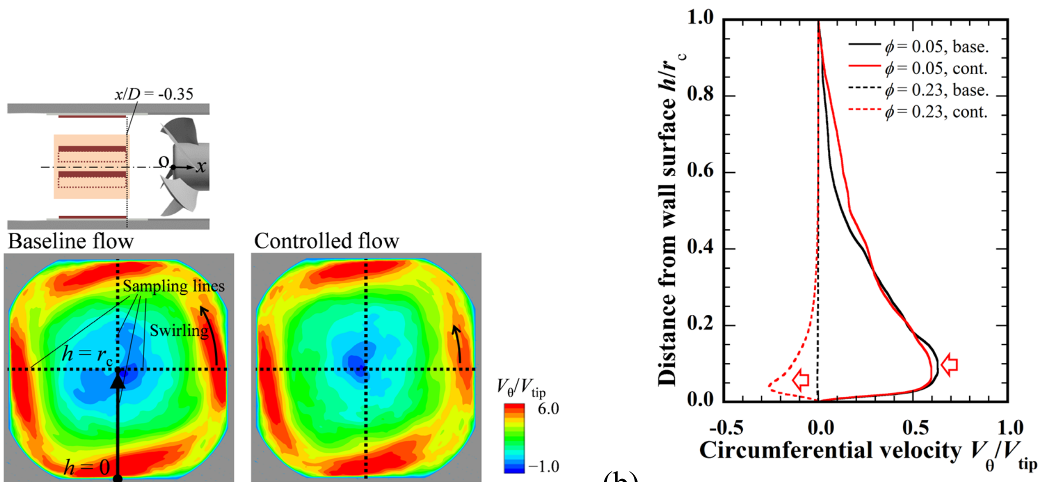

(a) (b)

Fig. 14. Predicted mean circumferential velocity V_θ in inflow to fan (x/D = −0.35) for baseline and controlled flows. (a) Contours of mean circumferential velocity at ϕ = 0.05. (b) Profiles of mean circumferential velocity along normal lines of four duct walls shown with broken lines in Fig. (a), where values along four lines are averaged.

4.4.2 Turbulence and Vortices in Inflow to Fan

Figure 15(a) shows the baseline and controlled profiles of mean axial velocity U upstream of the fan at ϕ = 0.05 and 0.23. The reverse flow occurred particularly near the duct walls at the low flow rate of ϕ = 0.05, which caused the intense swirling flow as shown in Fig. 14. This reverse flow near the duct wall was weakened by the control, as shown in Fig. 15(a). These effects were similar to the suppression effects of the flow separation around an airfoil using streamwise plasma actuators [28]. Meanwhile, the axial velocity decreased at some positions distant from the duct wall owing to the suppression of the reverse flow near the duct wall under the condition of a constant overall flow rate. The axial velocity was increased near the duct wall at the high flow rate of $\phi = 0.23$, which also contributed to the increase in blade loading near the tip region as shown in Fig. 12.

Figure 15(b) shows the baseline and controlled turbulence intensities of the axial velocity, u_{rms}. The turbulence intensity was more intense at the low flow rate ($\phi = 0.05$) compared with the high flow rate ($\phi = 0.23$). This is because a reverse flow occurred at the low flow rate, as shown in Fig. 15(a), and flow disturbances near the fan affected the flow upstream of the fan [10]. As shown in Fig. 15(b), the inflow turbulence near the duct wall at the low flow rate was weakened by the control owing to the weakening of the reverse flow, as shown in Fig. 15(a). Meanwhile, the turbulence intensity intensified at a position distant from the duct wall, where the above-mentioned decrease in the mean axial velocity caused the flow disturbances near the fan to affect the upstream flow more intensely. This intensification of the inflow turbulence possibly led to a decrease in the static pressure coefficient and blade loading at low flow rates, as shown in Figs. 6 and 12, respectively.

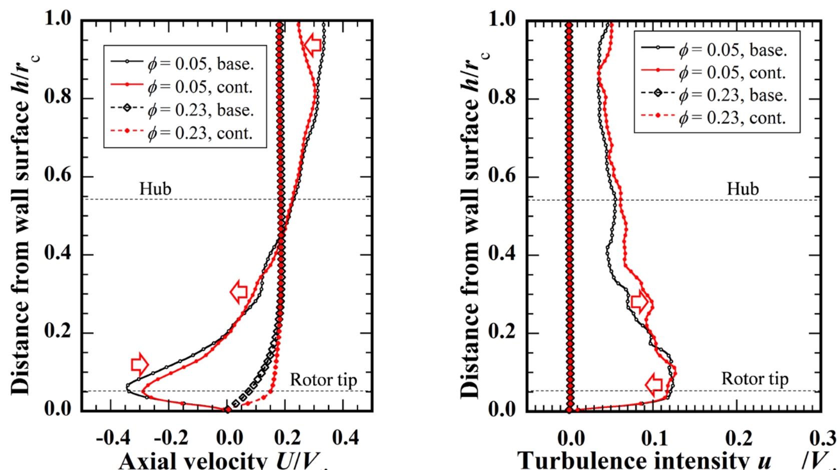

(a) (b)

Fig. 15. Predicted baseline and controlled profiles of axial velocity upstream of the fan ($x/D = -0.35$) at $\phi = 0.05$ and 0.23. (a) Profiles of mean axial velocity U. (b) Turbulence intensity of axial velocity u_{rms}.

Figure 16 shows the instantaneous iso-surfaces of the second invariant of the velocity gradient tensor, q, colored by the streamwise vorticity ω_x at the high flow coefficient of $\phi = 0.23$. In the baseline case, active vortices appeared only near the fan. In controlled flow, streamwise vortices were generated by the flow induced by the plasma actuators. These vortices promoted momentum transport from the freestream to the region near the duct wall, leading to an increase in the axial velocity, as shown in Fig. 15(a).

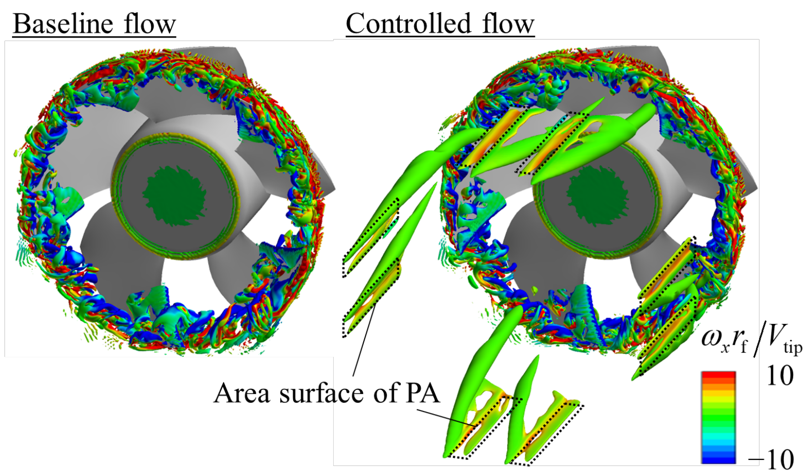

Fig. 16. Predicted iso-surfaces of the second invariant ($q/(V_{tip}/D)^2$) = 2.0) colored by streamwise vorticity ω_x at $\phi = 0.23$, where only the iso-surface in the upstream region of the fan ($x/D = -1.1 - 0$) are shown for clarity.

4.4.3 Rotor Wake

Figure 17 shows the baseline and controlled power spectra of the axial velocity fluctuations 1 mm downstream of the rotor blade tip (100% span). The power at the high flow rate of $\phi = 0.23$ was particularly along the curve of −5/3 power, which indicates the generation of a turbulent flow in the rotor wake. Moreover, the intense power at $f/nZ_b = 1.0$ indicated the periodic passage of the wakes of the rotor blades. The periodic interactions between the rotor wake and struts could intensify the radiation of tonal sounds related to the rotational speed [29].

As shown in Fig. 17, the power at $f/nZ_b = 1.0$ was slightly increased by the control at the high flow coefficient of $\phi = 0.23$, which was possibly related to the increase of the axial velocity around the tip region as shown in Fig. 15(a). Consequently, the periodic interactions between the rotor wake and the structures intensified, leading to a larger resonant sound at the harmonic frequency of the BPF, as shown in Fig. 10. Meanwhile, it is noted that the acoustic radiation can be slightly reduced, as shown in Fig. 13, by lowering the rotational speed under constant aerodynamic conditions of flow rate and pressure rise, utilizing the enhancement of the aerodynamic characteristics by the control at a high flow rate.

Figure 17 also shows that the power in the overall frequency range, including $f/nZ_b = 1.0$, was decreased by the control at the low flow coefficient of $\phi = 0.05$. This is possibly owing to the decrease in inflow turbulence around the tip region by the control, as shown in Fig. 15(b). This decrease in the power of the velocity fluctuations weakens the interactions between the rotor wake and struts, which contributes to the reduction in the resonant sound discussed in Subsection 4.2.

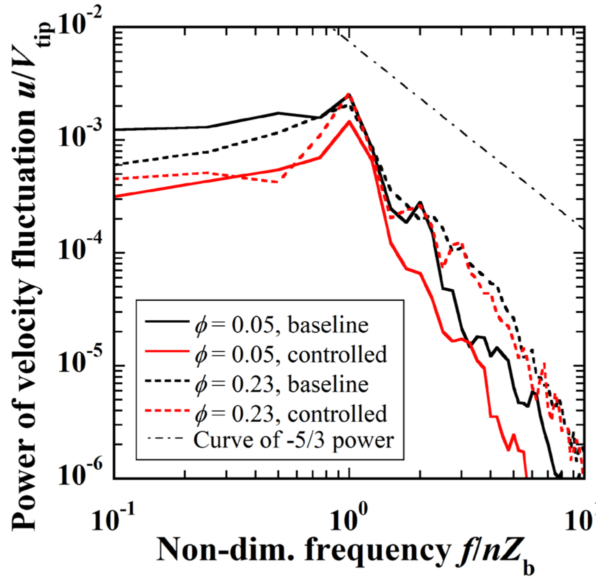

Fig. 17. Predicted power spectra of axial velocity fluctuations at 1 mm downstream position of blade tip (100% span) at $n = 60.0\ \mathrm{s}^{-1}$

5. Conclusions

In this study, direct aeroacoustic simulations and experiments were performed to investigate the effects of plasma actuators on controlling flows around an axial fan. Specifically, the induced flow was circumferentially directed in the reverse direction of fan rotation. The focus was on the control effects on acoustic radiation from the fan under duct resonance occurring at the harmonic frequency of the BPF, as well as the changes in aerodynamic characteristics and flow field around the fan caused by the control. The results revealed that the static pressure coefficient decreased and increased with the control at low and high flow coefficients, respectively. Based on this change of the aerodynamic characteristics, the tonal resonant sound at the harmonic frequency of the BPF was confirmed to be effectively reduced by controlling rotational numbers for the equivalent aerodynamic conditions of the flow rate and pressure rise, both at low and high flow rates.

Furthermore, it was observed that the axial velocity increased near the upstream duct wall, accompanied by the generation of vortices via control at a high flow coefficient. This resulted in an increase in the static pressure coefficient with an increase in the relative inflow angle, enabling the reduction of acoustic radiation by decreasing the rotational speed for the same pressure rise. At a low flow rate, the reverse flow and turbulence intensity near the upstream duct wall weakened, leading to the suppression of periodic interactions between the rotor wake and struts, consequently contributing to a reduction in resonant acoustic radiation at the first-harmonic frequency of the BPF.

Overall, this study clarified the control effects of circumferential jets using plasma actuators on aerodynamic sound from an axial fan for the first time. The insights gained into the flow fields with control are valuable for mitigating acoustic radiation and improving the aerodynamic characteristics of axial fans. Moreover, these findings are expected to contribute to the establishment of flow control in and around fluid machinery utilizing active flow control. As a future task, more efficient control methodology such as an intermittent control was necessary to be identified along the accurate evaluation of the power consumption.

ACKNOWLEDGEMENT

We gratefully acknowledge the computational resources provided by the HPCI System Research Project (Project ID: hp230012). This work was partially supported by JSPS KAKENHI (No. 21K03874, 24K07301). We also extend our sincere appreciation to Professor Hideki Yanada for his invaluable contributions and fruitful discussions throughout this research endeavor.

NOMENCLATURE

A	flow passage area of fan, m^2
C	chord length along tip, mm
D	outer side of casing, mm
$\boldsymbol{D}_{\mathrm{PA}}$	body force vector for plasma actuators
$\boldsymbol{E}$, $\boldsymbol{F}$, $\boldsymbol{G}$	inviscid flux vectors
$\boldsymbol{E}_{\mathrm{v}}$, $\boldsymbol{F}_{\mathrm{v}}$, $\boldsymbol{G}_{\mathrm{v}}$	viscous flux vectors
F_{PA}	magnitude of body force of plasma actuators, N/m^3
h	distance from duct wall, mm
n	rotational speed, s^{-1}
P	mean pressure, Pa
P_{p}, P_{s}	mean pressure on pressure and suction surfaces, Pa
$\boldsymbol{p}_{\theta}$	circumferential unit vector perpendicular normal vector of duct wall
p	Pressure, Pa
Q	flow rate, m^3/s
$\boldsymbol{Q}_{\mathrm{c}}$	vector of conserved variable
q	the second invariant of velocity gradient tensor, s^{-2}
r_{c}	inner radius of casing, mm

r_f	rotor radius, mm
r_h	hub radius, mm
Re	Reynolds number
T	time period, s
U	axial velocity, m/s
$\boldsymbol{V}$	volume penalization term
V_{pp}	driving voltage of plasma actuators, V
V_{tip}	tip velocity, m/s
V_{θ}	circumferential velocity, m/s
x	axial coordinate, m
x_c	non-dimensional coordinate along blade chord
y	vertical coordinate, m
z	coordinate normal to x, y-axes, m
Z_b	number of rotor blades

Greek Letters

Δ	difference
θ	angle in anti-clockwise direction from upstream view, deg
θ_b	angle of blade surface, deg

ν	kinematic viscosity, m^2/s
ρ	fluid density, kg/m^3
σ	tip clearance, mm
Υ	parameter of volume penalization method
ϕ	flow coefficient
χ	mask function
ψ	static pressure coefficient
ω_x	streamwise vorticity, s^{-1}

Appendix A: Uncertainty of Measurement Equipment

The sources of uncertainty for the flow coefficient were the uncertainties of a differential pressure gauge for an orifice flowmeter and the evaluation of ambient density using a barometer with a thermometer (BAROMEX 7612-00, Sato Keiryoki). The uncertainties of the pressure gauge, barometer, and thermometer were 0.02 Pa, 1% of the atmospheric pressure, and ±1 K, respectively. These lead to an evaluation uncertainty of ±0.005 kg/m^3 for the ambient density and ±0.0002 m^3/s for the flow rate. The uncertainty of the rotational speed is 0.23 s^{-1} at the rotational speed of n = 60.0 s^{-1}, which corresponds to the uncertainty of 0.027 m/s in the tip velocity.

Appendix B: Measurements of Induced Flow by Plasma Actuator(s)

The velocity fields of the flows induced by one and two plasma actuators set on a wide flat wall (100×100 mm^2) were measured using particle image velocimetry (PIV) with the setup shown in Fig. B1. A YAG laser (CW532-5WMUT, 5 W, Kanomax) was used to generate a laser sheet with a thickness of 3 mm along a plane perpendicular to the electrodes of the plasma actuators. Water misty particles with an average size of 4.6 μm were used as tracers with the mist generation (KN-80S, Shin-Ei Industries). The PIV images were captured at a frame rate of 1 kHz and a shutter speed of 1 ms using a high-speed camera (FASTCAM Mini AX100, Photoron). The cross-correlation between serially captured images (1024×880 pixels, 0.06 mm/pixel) was calculated for the interrogation area of 8×8 pixels in the PIV analysis. The obtained spatial resolution of the velocity fields was 0.46 mm.

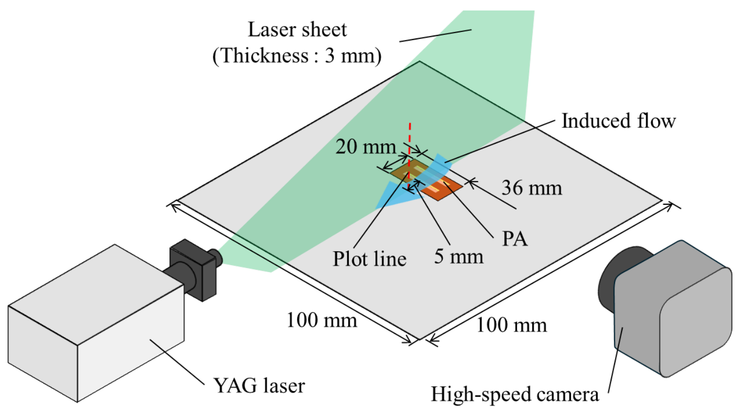

Fig. B1. Measurement of induced flow by plasma actuators using PIV.

References

[1] Tyler, J. M., and Sofrin, T. G., 1962, "Axial Flow Compressor Noise Studies," SAE Trans., **70**, pp. 309–332. DOI: 10.4271/620532

[2] Mugridge, B. D., and Morfey, C. L., 1972, "Sources of Noise in Axial Flow Fans," *J. Acoust. Soc. Am*., **51**, pp. 1411–1426. DOI: 10.1121/1.1912992

[3] Louw, F. G., 2015, "Investigation of the Flow Field in the Vicinity of an Axial Flow Fan During Low Flow Rates," Ph. D. thesis in Stellenbosch University.

[4] Longhouse, R. E., 1978, "Control of Tip-Vortex Noise of Axial Flow Fans by Rotating Shrouds," J. Sound Vib., **58**(2), pp. 201–214. DOI: 10.1016/S0022-460X(78)80075-3

[5] Lin, S. C., and Chou, C. A., 2004, "Blockage Effect of Axial-Flow Fans Applied on Heat Sink Assembly," Appl. Therm. Eng., **24**(16), pp. 2375–2389. DOI: 10.1016/j.applthermaleng.2004.03.009

[6] Yokoyama, H., 2023, "Fluid-Acoustic Interactions with Resonance Around an Axial Fan in a Duct," Proceedings of Flinovia IV, Sydney, Australia.

[7] Naitong, L., Changyoung, J., Lixi, H., and Chen, W., 2021, "Effect of Porous Casing on Small Axial-Flow Fan Noise," Appl. Acoust., **175**, 107808. DOI: 10.1016/j.apacoust.2020.107808

[8] Tingsheng, Z., Cheng, Y., and Åbom, M., 2023, "Tonal Noise Reduction of an Electric Ducted Fan Using Over-the-Rotor Acoustic Treatment," Appl. Acoust., **205**, 109298. DOI: 10.1016/j.apacoust.2023.109298

[9] Itagaki, R., Minowa, K. and Yokoyama, H., 2018, "Effects of Slits of Casing on Aeroacoustic Noise Radiated from an Axial Fan," Proceedings of ICSV 25, Hiroshima, Japan, pp. 1383–1390.

[10] Yokoyama, H., Minowa, K., Orito, K., Nishikawara, M., and Yanada, H., 2020, "Compressible Simulation of Flow and Sound Around a Small Axial-Flow Fan with Flow through Casing Slits," J. Fluids Eng., Trans. ASME, **142**, 101215. DOI: 10.1115/1.4047807

[11] Neuhaus, L., and Neise, W., 2005, "Active Control to Improve the Aerodynamic Performance and Re-duce Tip Clearance Noise of Axial Turbomachines," Proceedings of 26th AIAA Aeroacoustics conference, Monterey, California, AIAA 2005-3073. DOI: 10.2514/6.2005-3073

[12] Jukes, T. N., and Choi, K., 2009, "Flow Control Around a Circular Cylinder Using Pulsed Dielectric Barrier Discharge Surface Plasma," Phys. Fluids, **21**(8), 084103. DOI: 10.1063/1.3194307

[13] Greenblatt, D., Pfeffermann, O, Keisar, D., and Göksel, B., 2021, “Wells Turbine Stall Control Using Plasma Actuators,” AIAA J., **59**, pp. 765–772. DOI: 10.2514/1.J060278

[14] Saddoughi, S., Bennett, G., Boespflug, M., Puterbaugh, S. L., and Wadia, A. R., 2015, “Experimental Investigation of Tip Clearance Flow in a Transonic Compressor with and without Plasma Actuators,” J. Turbo., Trans. ASME, **137**, pp. 207-217. DOI: 10.1115/GT2014-25294

[15] Yokoyama, H., Otsuka, K., Otake, K., Nishikawara, M., and Yanada, H., 2020, “Control of Cavity Flow With Acoustic Radiation by an Intermittently Driven Plasma Actuator,” Phys. Fluids, **32**(10), 106104. DOI: 10.1063/5.0017658

[16] Inasawa, H., Ninomiya, C., and Asai, M., 2013, “Suppression of Tonal Trailing-Edge Noise from an Air-Foil Using a Plasma Actuator,” AIAA J., **51**(7), pp. 1695–1702. DOI: 10.2514/1.J052203

[17] Yokoyama, H., Yoza, K, Nishikawara, M., and Yanada, H., 2023, “Simulation of Acoustic Oscillatory Flows Around a Curvature Controlled by a Plasma Actuator,” Appl. Acoust., **205**, 109274. DOI: 10.1016/j.apacoust.2023.109274

[18] Abernethy, R. B., Benedict, R. P., and Dowdell, R. B., 1985, “ASME Measurement Uncertainty,” ASME J. Fluids Eng., **107**(2), pp. 161–164. DOI: 10.1115/1.3242450

[19] Lele, S. K., 1992, “Compact Finite Difference Schemes With Spectral-Like Resolution,” J. Comput. Phys., **103**(1), pp. 16–42. DOI: 10.1016/0021-9991(92)90324-R

[20] Liu, Q., and Vasilyev, O. V., 2007, “A Brinkman Penalization Method for Compressible Flows in Complex Geometries,” J. Comput. Phys., **227**(2), pp. 946–966. DOI: 10.1016/j.jcp.2007.07.037

[21] Yokoyama, H., Miki, A., Onitsuka, H., and Iida, A., 2015, “Direct Numerical Simulation of Fluid-Acoustic Interactions in a Recorder with Tone Holes,” J. Acoust. Soc. Am., **138**(2), pp. 858–873. DOI: 10.1121/1.4926902

[22] Tanaka, Y., Yokoyama, H., and Iida, A., 2018, “Forced-Oscillation Control of Sound Radiated from the Flow Around a Cascade of Flat Plates,” J. Sound Vib., **431**, pp. 248–264. DOI: 10.1016/j.jsv.2018.06.013

[23] Gaitonde, D. V., and Visbal, M. R., 2000, “Pade-Type Higher-Order Boundary filters for the Navier-Stokes equations,” AIAA J., **38**(11), pp. 2103-2112. DOI: 10.2514/2.872

[24] Matsuura, K., and Kato, C., 2007, “Large-Eddy Simulation of Compressible Transitional Flows in a Low-Pressure turbine cascade,” AIAA J., **45**(2), pp. 442–457. DOI: 10.2514/1.22425

[25] Fukuma, A., Kawai, M., Furukawa, N., Kawasaki, K., Yamagiwa, I., Nishikawara, M., and Yokoyama, H., 2024, Fluid-Acoustic Interactions Around an Expanding Pipe with Orifice Plates, Phys. Fluids, **36**(3), 036116. DOI: 10.1063/5.0193029

[26] Roache, P. J., 1994, "Perspective: A Method for Uniform Reporting of Grid Refinement Studies," J. Fluids Eng. Trans. ASME, **116**(3), pp.405–413. DOI: 10.1115/1.2910291

[27] Kim, J. W., and Lee, D. J., 2000, "Generalized Characteristic Boundary Conditions for Computational Aeroacoustics," AIAA J., **38**(11), pp. 2040–2049. DOI: 10.2514/2.891

[28] Timothy, N. J., Segawa, T., and Furutani, H., "Flow Control on a NACA 4418 Using Dielectric-Barrier-Discharge Vortex Generators," AIAA J., **51**(2), pp.452–464. DOI: 10.2514/1.J051852

[29] Minowa, K., Yokoyama, H., Orito, K., and Iida, A., 2019, "Direct Aeroacoustic Simulation of Flow and Noise Around an Axial-Flow Fan Regarding Effects of Slits in a Casing," Proceedings of 26th International Congress on Sound and Vibration, Montreal, Canada, 346

Figure Captions List

Fig. 1 Axial fan with five rotor blades housed in casing with four struts.

Fig. 2 Experimental setup for control of flow around a fan with plasma actuators, wherein an axial fan is installed in a duct (with a square flow passage having side of D = 40 mm).

Fig. 3 Schematics of control by plasma actuators upstream of the fan.

Fig. 4 Computational domain with boundary conditions.

Fig. 5 Comparison of measured and predicted velocity fields of induced flow by one and two plasma actuators on a wide flat plate. (a) Setup of plasma actuators. (b) Measured and predicted velocity profiles 5 mm downstream of the plasma actuators.

Fig. 6 Measured and predicted variations of static pressure coefficient with flow coefficient for baseline and controlled flows at $n = 60.0\ \mathrm{s}^{-1}$.

Fig. 7 Measured and predicted sound pressure spectra ($x/D = -2.5$) with and without control at $n = 60.0\ \mathrm{s}^{-1}$ and $\phi = 0.05$, where variances of measured level with the same averaging number as that of the computation are represented with bars.

Fig. 8 Measured baseline sound pressure spectra at $x/D = -2.5$ for $\phi = 0.17$, in which the frequency resolution is $\Delta f/nZ_b = 1/256$ corresponding to Δf = 0.98, 1.17, 1.37 Hz for n = 50.4, 60.0, 70.0 s^{-1}, respectively.

Fig. 9 Predicted contours of fluctuations pressure without control at $n = 60\ s^{-1}$ and $\phi = 0.05$, where $t = 0$ is time for the highest fluctuation pressure in the upstream duct and T is time period of resonance frequency.

Fig. 10 Measured and predicted variations of the level difference of baseline and controlled resonant sounds at $2nZ_b$ with flow coefficient ($n = 60.0\ s^{-1}$, $x/D = -2.5$), where variances of level in four tests are indicated with bars for measured data.

Fig. 11 Predicted contours of fluctuating pressure in and around the upstream duct for controlled flow at $\phi = 0.05$ and $n = 60.0\ s^{-1}$.

Fig. 12 Predicted blade loading along 80% span for baseline and controlled flows with $\phi = 0.05$ and 0.23, where $x_c = 0.0$ and 1.0 correspond to leading and trailing edges, respectively.

Fig. 13 Levels of resonant sound at $2nZ_b$ in controlled flows with adjusted rotational speeds of $n = 63.0$ and $57.0\ s^{-1}$ for the same flow rate and static pressure as those in the baseline case at $\phi = 0.05$ and 0.23 at $n = 60.0\ s^{-1}$, respectively, along baseline levels.

Fig. 14 Predicted mean circumferential velocity V_θ in inflow to fan ($x/D = -0.35$) for baseline and controlled flows. (a) Contours of mean circumferential velocity at $\phi = 0.05$. (b) Profiles of mean circumferential velocity along normal lines of four duct walls are shown with broken lines in Fig. (a) at $\phi = 0.05$ and 0.23, where values along four lines are averaged.

Fig. 15 Predicted baseline and controlled profiles of axial velocity upstream of the fan (x/D = –0.35) at ϕ = 0.05 and 0.23. (a) Profiles of mean axial velocity U. (b) Turbulence intensity of axial velocity u_{rms}.

Fig. 16 Predicted iso-surfaces of the second invariant ($q/(V_{tip}/D)^2$) = 2.0) colored by streamwise vorticity ω_x at ϕ = 0.23, where only the iso-surface in the upstream region of the fan (x/D = –1.1 – 0) are shown for clarity.

Fig. 17 Predicted power spectra of axial velocity fluctuations at 1 mm downstream position of blade tip (100% span) at n = 60.0 s^{-1}.

Fig. B1 Measurement of induced flow by plasma actuators by PIV.